CHAPTER 3

Efficient Designs of Double-pass Curved Solar Air Heaters

Recent research has shown that flat plate double-pass solar air heaters (DPSAH) exhibit higher thermal performance compared to conventional flat plate single-pass solar air heaters (SPSAH). However, scientific literature on design and performance evaluation of a curved DPSAH is scarce. In this chapter, we systematically investigated various designs of DPSAH and reported its performance characteristics using a validated numerical model. Higher outlet air temperature by about 5°C was observed when the DPSAH absorber plate is located at the mid of the insulating wall and transparent glass cover. Furthermore, putting asymmetric semi-circular roughened surfaces shows better performance than symmetric circular shapes as the reattachment of vortices with the absorber plate is more frequent in the former case. Two new correlations were developed for Nusselt number (Nu) and friction factor $\left(f\right)$ as a function of Reynolds number (Re) and relative roughness height (d/H). The values of (Nu) and $\left(f\right)$ obtained from the developed correlations agree well with data from the mode.

3.1 Introduction

Since the last few decades, renewable energy has become an essential resource of energy because of the oil crisis, huge energy demand, its availability for a long period, and less adverse effect on the environment and health. Among all the renewable Fig.3.1 resources of energy, solar energy is available in abundance; it is cheap and clean. The air heated by the solar energy has wide applications such as room heating, desalination, drying for agriculture and industrial products (grains, fish, wood, paper and food factories etc.)[103].Solar air heating systems such as solar air heaters (SAHs) are among the most acceptable devices for domestic and commer-

cial applications. Apart from their simple design, low manufacturing cost, and no moving parts, the most important attribute that has attracted researchers across the globe is that they are very much flexible for design modifications. However, one major drawback of the existing designs is low collection efficiency because of the poor convective heat transfer coefficient between the absorber plate and flowing air. That's why various efforts have been made by researchers to enhance its efficiency by using a double flow channel instead of a single flow channel (parallel, counter and recycle)[12, 58, 118, 142],curved channel in place of straight channel [87, 123, 124], fin with baffle [46, 49, 148], corrugated absorber[22, 47, 63], artificial roughness [21, 57, 60, 81] and packed bed [23, 120],etc.

Single flow and double flow channel SAH are also known as single-pass and double-pass SAH, respectively. In a SPSAH, air flows between the glass and absorber plate or absorber and bottom plate while in DPSAH, air flows in two channels, i.e., above and below the absorber plate. Based on the previous investigations, DPSAHs are found to be thermally better than SPSAHs because of the high heat extraction rate from the absorber plate, top minimum losses, and increased flow interaction due to double heat transfer area [27, 149]. It has been reported that the thermal efficiency of a DPSAH is 10-15% higher as compared to single-pass SAHs for different range operating conditions [118, 142].

Recently[87, 124], the flat plate design of SAH was transformed to a curved smooth channel for enhancing the thermal performance. Due to centrifugal forces, secondary flow vortices in the curved channel were observed as a result of forcing the mean flow velocity near the absorber plate.This enhanced the heat transfer rate. Singh and Singh [124] reported that "thermohydraulic performance of a conventional flat plate solar air heater can be increased without incorporating any extended surfaces if a flat parallel plate is transformed into curved designs". It was reported that curved design is about 40% thermally more effective than the conventional flat plate natural convection SAH.The numerical investigations in a curved SPSAH with different shapes of down configuration ribs (half-triangular, half-trapezoidal and quarter-circle) have investigated by the same group[122].It was reported that ribs with sharp edged shapes offer high thermal performance at the expense higher hydrodynamic losses in the system. Circular ribs offer a good balance between thermal and hydraulic performance. Therefore, investigations using circular and semi-circular ribs has been presented in this paper. As mentioned earlier, numerous works are available on performance enhancement of DPSAH.Some relevant literature has been listed in Table 3.1.

Table 3.1: List of the relevant literature of double-pass solar air heater having various roughness geometry and flow arrangement. Notice that rectangular designs of DPSAHs.

Investigators	Type of flow	Upper and lower cross-section	Extended surface	Findings

Table 3.1: List of the relevant literature of double-pass solar air heater having various roughness geometry and flow arrangement. Notice that rectangular designs of DPSAHs.

Ho et al.[46]	Double-flow with external recycle SAH	Rectangular	Rectangular fin	• Recycled + fin + baffle SAH has maximum collector efficiency • Efficiency increase with the increase in mass flow rate and recycle ratio
Yeh et al. [147]	Double -flow SAH	Rectangular	symmetrical rectangular fin	• Maximum collector efficiency occurs at a mass flow rate fraction of 0.5 • Collector efficiency increases with the mass flow rate.
Gabhane and Patil[32]	Double-flow SAH	Rectangular	symmetrical Multiple C-shaped ribs	• $Nu = 0.206\,(Re)^{0.81}\,(P/e)^{-0.037}\,(\alpha/90)^{0.27}$ • $f = 0.91\,(Re)^{-0.28}\,(P/e)^{-0.15}\,(\alpha/90)^{-0.12}$
Ozgen et al.[104]	Double-flow SAH	Rectangular	Staggered and un-staggered arrangement cans	• Maximum collector efficiency in a un-staggered arrangement. • Maximum collector efficiency with a mass flow rate of 0.05 kg/s.
Esen[31]	Double-flow SAH	Rectangular	Triangular (Type - IV),Triangular with bend upper vertices (Type-III) and Rectangular with v cut (Type-II) shape fins	• Type-III(state-II) has maximum second law efficiency of 60.97% for 0.025 kg/s. • The optimum value of efficiency is middle level (state-II) ofthe absorber in cross-section.

Table 3.1: List of the relevant literature of double-pass solar air heater having various roughness geometry and flow arrangement. Notice that rectangular designs of DPSAHs.

El-sebaii et al[29]	Double- flow SAH	Rectangular	V corrugated absorber	• The thermal efficiency of V-corrugated DPSAH was 14% higher than the flat plate DPSAH.
El-sebaii et al[30]	Double-flow SAH	Rectangular	unsymmetrical finned and V-corrugated absorber	• The thermal efficiency of V-corrugated was 9.3-11.9% more than the finned plate.
Sivakandhan et al.[134]	Double- flow SAH	Rectangular and triangular	Inclined shape of a rib	• Thermal and effective efficiency of hybrid parallel pass SAH were 22.4% and 18.1% times to conventional rectangular duct parallel pass SAH
Ramani et al.[112]	Double pass counter flow SAH	Rectangular	porous material in the lower channel	• The thermal efficiency of DPSAH with porous material is 20-25%higher than DPSAH without porous.
Hernandez and Quinonez[45]	Parallel flow, counter flow SAHs	Rectangular		• During the 10h period and the same climate condition, the thermal efficiency of Single-pass SAH, parallel DPSAH and counter DPSAH were 46%, 51%, and 57%, respectively.

It can be noticed that most of the investigations have been done in DPSAH with conventional

rectangular channel designs. Different shapes of extended surfaced on solar collector surface have been used to enhance the heat transfer rate. Even though numerous literature is available in DPSAH in rectangular channels designs, however, the performance investigations in a curved DPSAH is scarce. Symmetrical designs of protruded surfaces are preferred in the conventional DPSAH (see Table3.1).Whether symmetric or asymmetric roughened surfaces perform better in a curved DPSAH has been reported in this paper. Location of absorber plate play a significant role in DPSAH[30, 31, 147]. However, geometric optimization of absorber location with roughened surfaces in a curved DPSAH is yet to be investigated. Finally, no standard correlations are available for Nusselt number and friction factor prediction in a curved DPSAH. Keeping these deficiencies and ever-increasing energy needs in mind, a detailed investigation has been reported for various design configurations using an experimentally validated numerical model.

3.2 Numerical model

A two-dimensional, unsteady, and incompressible numerical model was developed for curved DPSAH (with semicircular and circular ribs). The Navier-Stokes equation was discretized using a finite volume method and SIMPLE algorithm was used to solve the coupled pressure and velocity fields[105].A detailed description of various designs, mesh generation, boundary conditions, and experimental validation are being discussed in the following subsections.

3.2.1 *Computational flow domain*

Due to lower resistance offered by the smooth circular/semicircular shape ribs in the curved design of SAH, details investigations have been conducted for the system shown in Fig.3.1 .The SAH has an inlet and outlet section, top transparent glass cover, absorber plate of length (L), and insulating bottom surface. The absorber plate is exposed to uniform solar radiation of 800 W/m^2.Air enters from the inlet section and exit from the outlet section. The flow split is into two streams on either side of the absorber plate. The present study has been divided into three sections: (1)the effect of the shape of ribs (circular and semicircular) (2)rib size and (3)absorber plate location optimization. Based on the absorber plate location, we term these three categories as SAH-I, SAH-II, and SAH- III. The necessary design and operating parameters used in the model are given in Table3.2.

3.2.2 *Mesh generation, grid-independent, and time-independent study*

A very fine mesh was created near the absorber plate and ribs to capture the boundary layer gradients while coarse mesh was used away from the absorber surface (Fig.3.2). It helps in optimizing computational time and resources. An unstructured mesh was adopted. As unstruc-

Table 3.2: Range of parameters for numerical modeling.

Parameters	Range
Absorber plate length, L	1600 mm
Height of duct, H	40 mm
Hydraulic diameter of the duct, D	77 mm
Rib diameter, d	4,6,8 and 10 mm
Rib pitch,P	30 mm
Location of absorber plate from glass, y	10, 20 and 30 mm
Relative roughness height,d/H	0.1, 0.15, 0.20 and 0.75
Relative roughness pitch, P/H	0.75
Relative location of absorber plate, y/H	0.25,0.5 and 0.75
Rib shape, S	Circular and Semicircular
Heat flux,q	800 W/m^2
Prandtl number, Pr	0.72
Reynolds number, Re	5000-10000 (6 values)
Curvature angle, α	25°
Convective heat transfer coefficient at top glass cover	$h = 5.7+3.8V_{\infty}(W/m^2)$
Channel width of duct, W	1000 mm

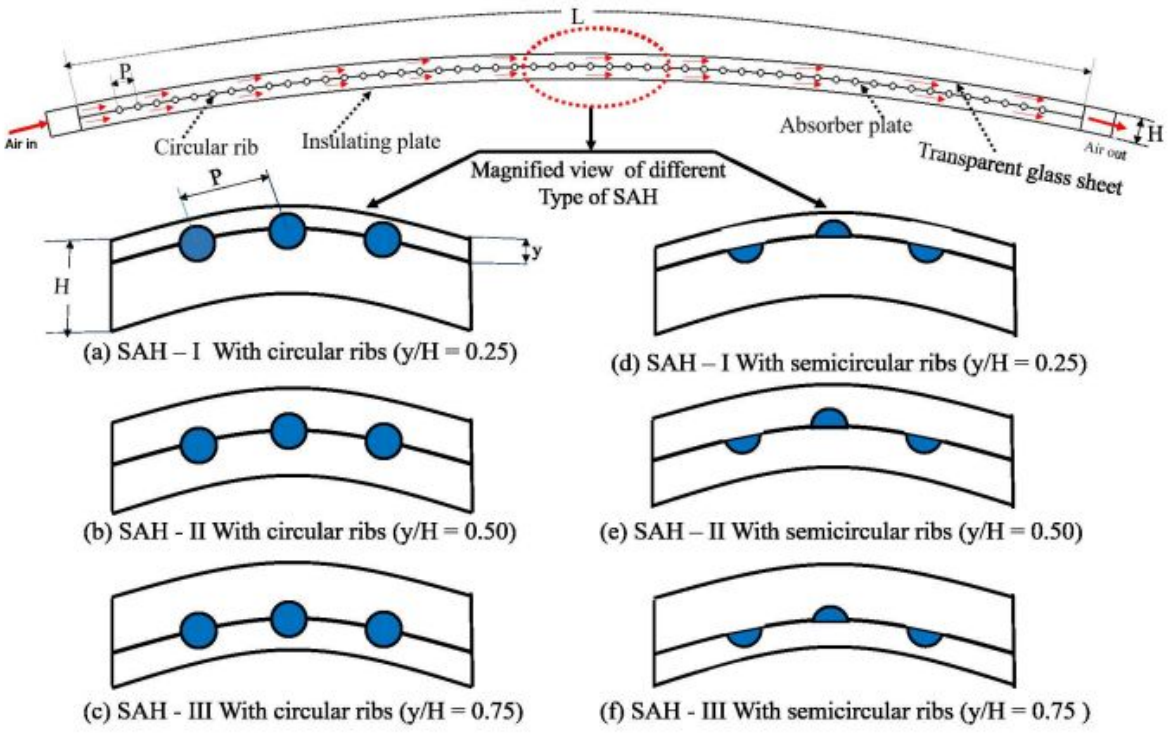

Figure 3.1: Schematic diagram of curved DPSAH with variable relative location of the absorber plates (y/H). Pitch P is kept constant in all the designs.

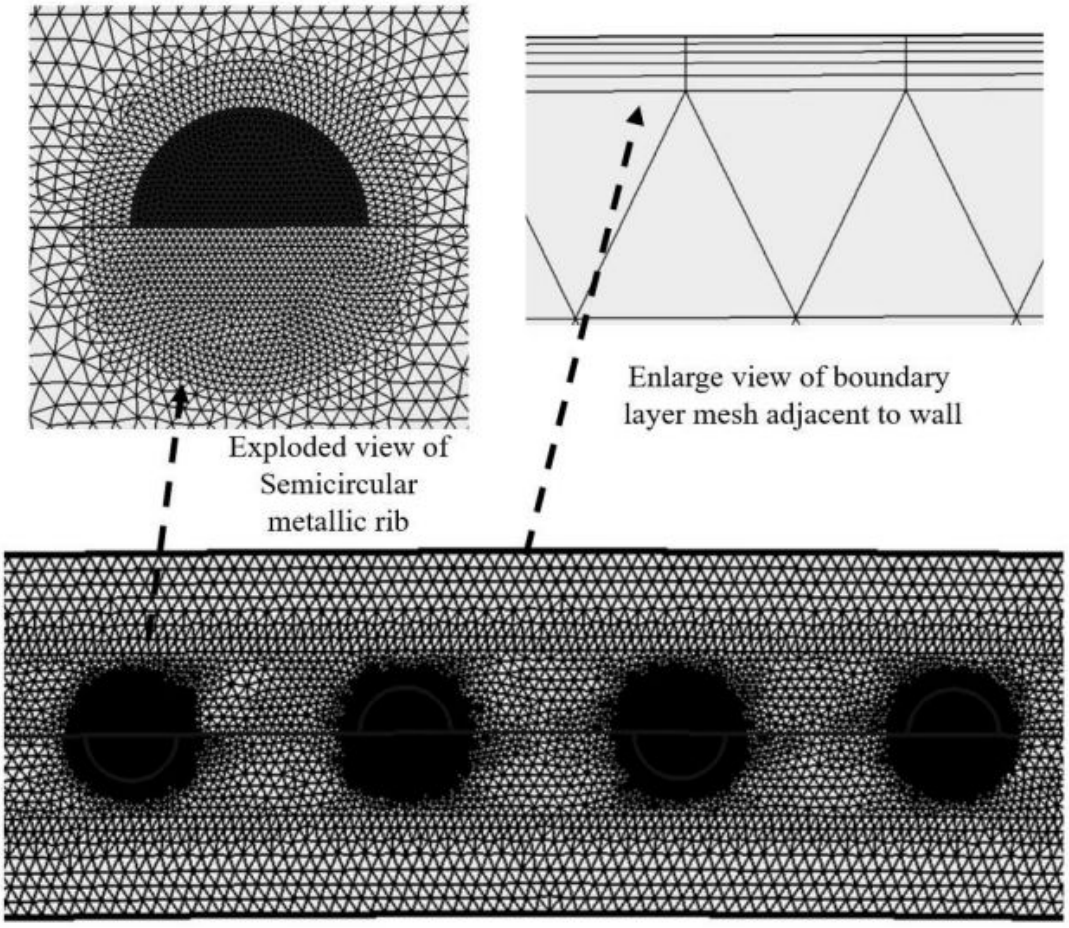

Figure 3.2: Two-dimensional unstructured mesh of SAH-II with semicircular metallic ribs.

tured mesh had an advantage over structured mesh in terms of capturing the secondary vortices for complicated geometry [35, 125].

3.2.2.1 *Grid independent test*

In grid independent study, SAH -III having circular rib with relative roughness height $^{d}/_{H}$ =0.1, relative roughness pitch $^{P}/_{H}$ =0.75 and curvature angle 25° was modeled for the number of elements in the range of 185660-1527627 under the same operating condition. The percentage deviation in Nusselt number (Nu) is evaluated and reported in Table3.3. The relative deviation in the Nusselt number is less than 0.35% from 218000 to 656000 grids. Based on the results, around 656000 elements were used in further simulations.

3.2.2.2 *Time independent study*

The time independent study was executed by using 656098 elements for the SAH -III at Reynolds number of 5000. The time independent study was conducted for four different time steps, which

Table 3.3: Grid independent study

S. No	Number of element	Nusselt number	Percentage variation in Nusselt number (Nu)
1	185660	24.89	-
2	218446	25.61	2.89
3	656098	25.70	0.35
4	1527627	25.72	0.07

Table 3.4: Time independent study.

S.No	Time step (second)	Number of element cell	Nusselt number (Nu)	% Variation in Nusselt number (Nu)
1	0.25	6.56×10^5	23.41	--
2	0.125		25.17	9.81
3	0.0625		26.38	2.60
4	0.0312		26.49	0.41

is shown in Table 3.4. The percentage change in Nu is 0.416% when time step changed from 0.0625 s to 0.0321 s. Based on the results, time step 0.0625 s was chosen for further investigations.

3.2.3 *Boundary condition*

Velocity inlet and pressure outlet boundary conditions are applied at the inlet and outlet section, respectively. Initially, the temperature of the working fluid at the inlet section and the whole domain is assumed to be at 300 K. Air properties do not change significantly in the range of observed temperature variations. Therefore, thermo-physical properties of air and absorber plate are assumed to be constant and given in Table 3.5. No-slip boundary condition was as-

Table 3.5: Constant thermo-physical properties of working fluid and absorber plate employed for numerical simulation.

Properties	Working fluid (air)	Absorber plate (Aluminum)
Density, $\rho\ (kg/m^3)$	1.184	2702
Thermal conductivity, k (W/mK)	0.026	273
Specific heat, $C_p\ (J/kgK)$	1003	903
Dynamic viscosity, μ (Ns/m^2)	1.855×10^5	-

signed at the walls. It is assumed that the top glass surface is exposed to still air environment condition and lose heat through convection and radiation. The equivalent heat transfer coefficient (convection and radiation) value was imposed on the transparent surface of SAH[136].

3.2.4 *Governing equation*

The governing equation for the unsteady flow of air through the curved DPSAH is given below [1, 138].

Mass conservation equation:

$$\frac{\partial(\rho)}{\partial t} + \nabla.(\rho V) = 0 \tag{3.1}$$

Momentum conservation equation:

$$\frac{\partial(\rho u)}{\partial t} + \nabla.(\rho u V) = -\frac{\partial p}{\partial x} + \mu\nabla(\nabla.u) - \nabla.\left(\overline{u'V'}\right) + \rho g_x \tag{3.2}$$

$$\frac{\partial(\rho v)}{\partial t} + \nabla.(\rho v V) = -\frac{\partial p}{\partial y} + \mu\nabla(\nabla.v) - \nabla.\left(\overline{v'V'}\right) + \rho g_y \tag{3.3}$$

Energy conservation equation:

$$\frac{\partial(\rho T)}{\partial t} + \nabla.(\rho T V) = \nabla.\nabla((\Gamma + \Gamma_t)T) \tag{3.4}$$

Where Γ and Γ_t symbols denote molecular thermal diffusivity and turbulent thermal diffusivity, respectively and are given by

$$\Gamma = \mu/Pr \tag{3.5}$$

and

$$\Gamma_t = \mu_t/Pr_t \tag{3.6}$$

Transport equations used for Realizable $k-\varepsilon$ model, to determine turbulent kinetic energy (k) and turbulent dissipation rate (ε), for computational flow domain exploration are:

$$\frac{\partial(\rho k)}{\partial t} + \nabla.(\rho k V) = \nabla.\nabla\left(k\left(\mu + \frac{\mu_t}{\sigma_k}\right)\right) + G_k + G_b \tag{3.7}$$

and

$$\frac{\partial(\rho\varepsilon)}{\partial t} + \nabla.(\rho\varepsilon V) = \nabla.\nabla\left(\varepsilon\left(\mu + \frac{\mu_t}{\sigma_\varepsilon}\right)\right) - \rho C_{2\varepsilon}\frac{\varepsilon^2}{k + \sqrt{\vartheta\varepsilon}} - C_{1\varepsilon}\frac{\varepsilon}{k}C_{3\varepsilon}G_b \tag{3.8}$$

where G_k represent the generation of turbulent kinetic energy due to mean velocity gradient, G_b represent the generation of turbulent kinetic energy due to buoyancy and using the value of k and ε to calculate the value of turbulent dynamic viscosity (μ_t) as[1]

$$\mu_t = \rho C_\mu \frac{k^2}{\varepsilon} \tag{3.9}$$

where $C_{1\varepsilon}, C_{2\varepsilon}, C_{3\varepsilon} and C_\mu$ are turbulence constants given as $C_{1\varepsilon} = 1.44, C_{2\varepsilon} = 1.92, C_{3\varepsilon} = 0.33, C_\mu = 0.09, \sigma_k = 1.0, \sigma_\varepsilon = 1.3$.

Hydraulic diameter is calculated using the equation,

$$D = \frac{4A}{C} \tag{3.10}$$

Reynolds number is given by,

$$Re = \frac{Inertia force}{Viscous force} = \frac{\rho UD}{\mu} \tag{3.11}$$

Dean number and Reynolds number are related as,

$$D_n = Re\sqrt{\frac{D}{2R_c}} \tag{3.12}$$

Reynolds number (Re) and Dean number (D_n) are important dimensionless parameters which give the information about fluid flow characteristic, whether it is the laminar or turbulent flow[87].In the current study, the range of Reynolds and Dean number are 5000-10000 and 497-994, respectively, which comes under the turbulent regime [65].Hence, the turbulent flow model was used. Applying the first law of thermodynamics the average convective heat transfer coefficient (h) is calculated with the help of temperature data obtained from the model as,

$$Q_u = m\dot{C}_{pa}(T_0 - T_i) = hA_p(T_P - T_m) \tag{3.13}$$

where T_m is mean temperature, i.e., (arithmetic mean of T_0 and T_i).

Average Nusselt number is represented as

$$Nu = \frac{hD}{k_a} \tag{3.14}$$

Darcy-Weisbach equation was used to calculate Darcy friction factor f, i.e.,

$$f = \frac{2\triangle pD}{L\rho U^2} \tag{3.15}$$

3.2.5 *Experimental validation of the model*

The developed numerical model was validated with the experimental result of Mahboub et al.[87].The authors [87] reported a new curved design of SAH. In the present model, the boundary conditions were imposed on the model to mimic the experimental setup of Mahboub et

al.[87].The same validation exercise was reported by the same authors [123].Since the same model is used here, we have presented it here for the sake of continuity. Fig.3.7 shows the comparison between experimental and numerical values of outlet air temperature T_0 as a function of solar radiation (I). The percentage error in outlet air temperature was evaluated as follow:

$$Relative\ error = \frac{(T_0 - T_i)_{Numerical} - (T_0 - T_i)_{Experimental}}{(T_0 - T_i)_{Experimental}} \tag{3.16}$$

Therefore, average absolute deviation between experimental and numerical values of outlet air temperature has been found to be 9.4%, which is under an acceptable limit.

3.3 Results and discussions

Thermal and hydraulic performance for the three categories of SAH shown in Fig.3.1 have been discussed. Data reported in this section was used to develop a correlation (next section) for Nusselt number and friction factor variation.

3.3.1 *Circular vs. semicircular ribs: which is better?*

Fig.3.3 shows the variation of Nu with Re for different designs of curved DPSAH. It is noted that the maximum value of Nu is seen in SAH -II with semicircular ribs and the minimum value is observed in SAH -III with circular ribs. Moreover, it is observed that SAH with semicircular ribs are more effective in heat transfer than SAH with circular ribs.This observation might seem contrary to the general notion. Ribs design extending from both sides (circular in the present case) of the heated absorber plate may seem efficient. However, semicircular ribs show higher thermal performance. It happens because of the larger reattachment zone of the fluid between the ribs of SAH with semicircular design compared to SAH with circular ribs (see velocity magnitude contour Fig.3.3(b) and (c)). Therefore, the rate of heat transfer from the absorber plate with semicircular ribs is higher than the corresponding circular ribs. The absolute average percentage increase in Nusselt number is about 45% with semicircular ribs as compared to circular ribs for the same operating parameters.

The variation of average friction factor with Reynolds number for different types of SAH has been shown in Fig.3.4. It is seen that the values of friction factor are lower for SAH with semicircular ribs than SAH with circular ribs. Besides, the same characteristic of friction factor is observed with increase in Re for all SAH designs. The secondary vortices originated at downstream of the ribs (circular and semicircular) causes an extra loss of energy which increases friction factor. The magnitude of energy losses due to circular ribs is larger than semicircular ribs. Consequently, the values of friction factor are higher in SAH with circular ribs than SAH with semicircular ribs.

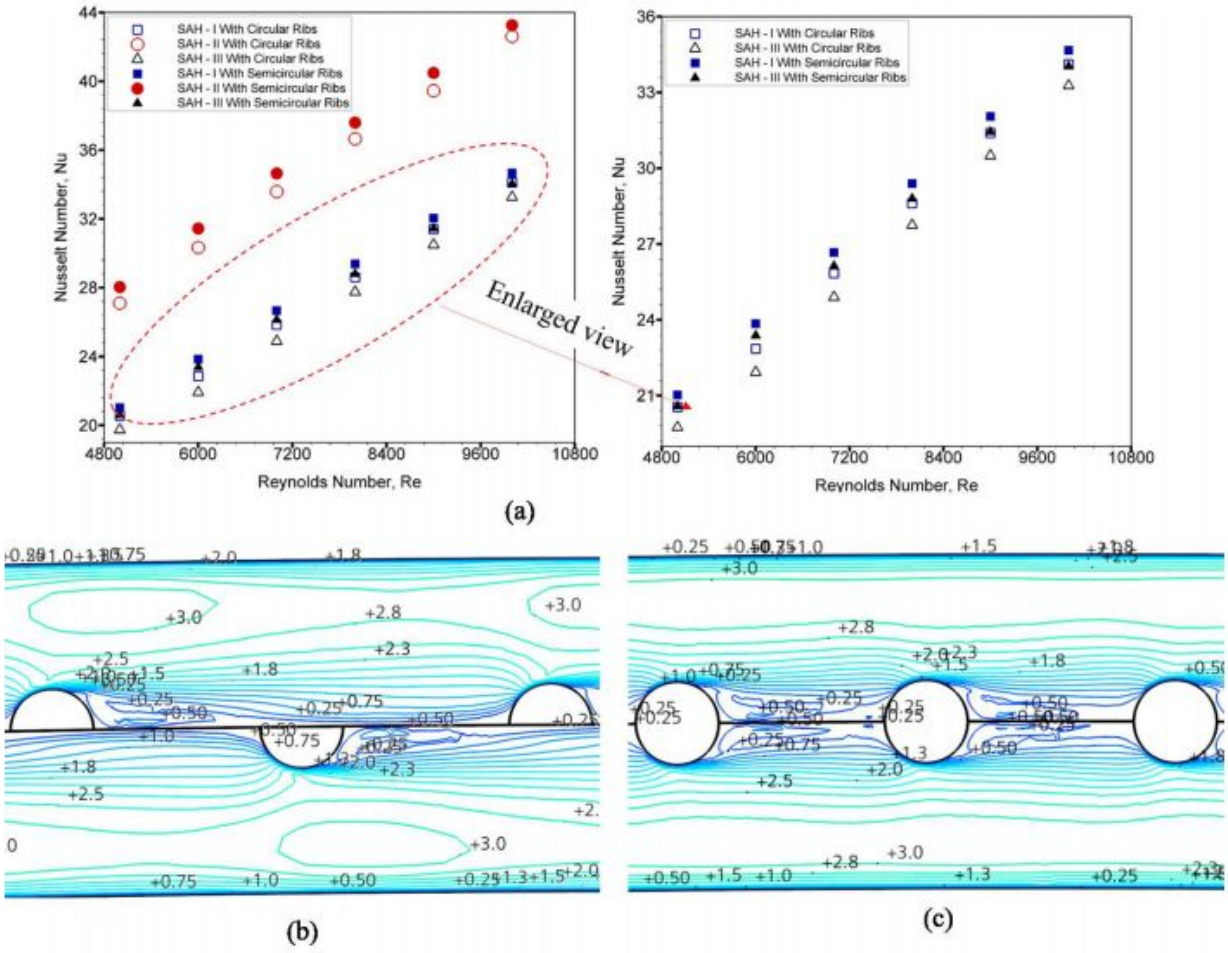

Figure 3.3: (a) Comparison of Nusselt number at various Reynolds number; contour of velocity magnitude of (b) SAH-II with semicircular ribs and (c) SAH-II with circular ribs at Re = 10,000 and $d/H = 0.25$.

For understanding the effect of shapes on local friction, local wall shear stress variation in SAH-II has been shown in Fig.3.6. The local maximum values of wall shear stress occur at the position of ribs due to the large velocity gradient. These values of local wall shear stress at semicircular ribs are higher than circular ribs surface due to high velocity gradient (see velocity contour in Fig.3.3 (b) and (c)). However, at other locations, the wall shear stress is significantly higher for circular ribs as compare to semicircular ribs. Consequently, the average value of wall shear stress in circular type SAH becomes higher than semicircular type SAH. High wall shear stress means higher-pressure drop, i.e., high flow resistance inside the SAH duct. Also, higher friction with circular ribs would increase the pumping power requirement, and with more materials needed for manufacturing, semicircular rib seems the best choice. In the subsequent subsection, the thermal performance of semicircular rib designs and their optimum location in DPSAH has been discussed.

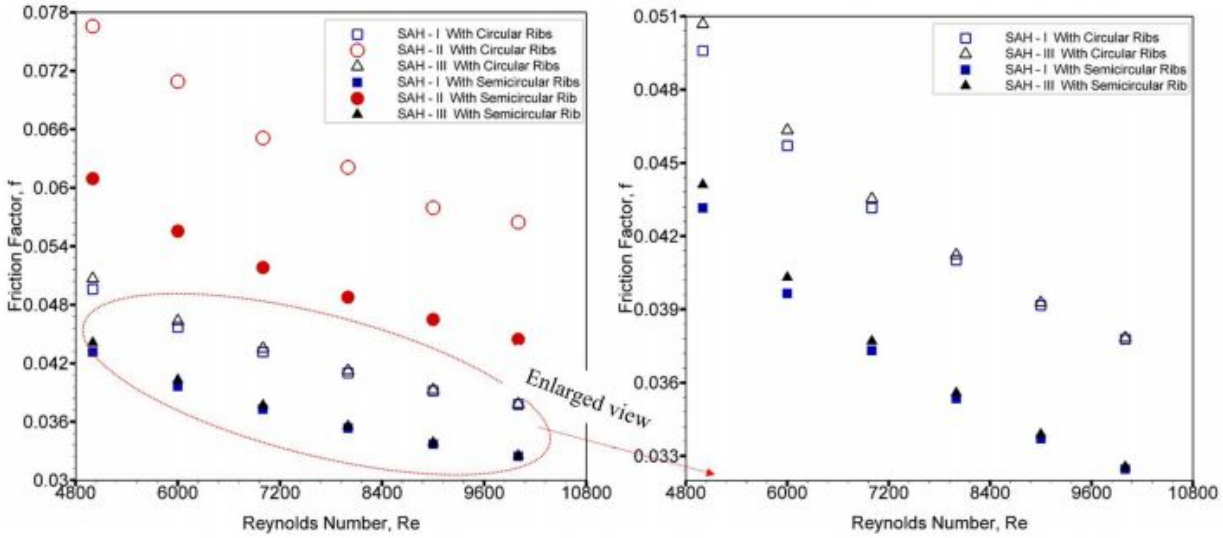

Figure 3.4: A plot of friction factor (f)versus Reynold number $(Re)$for a constant value of relative roughness height $(d/H)$of 0.15

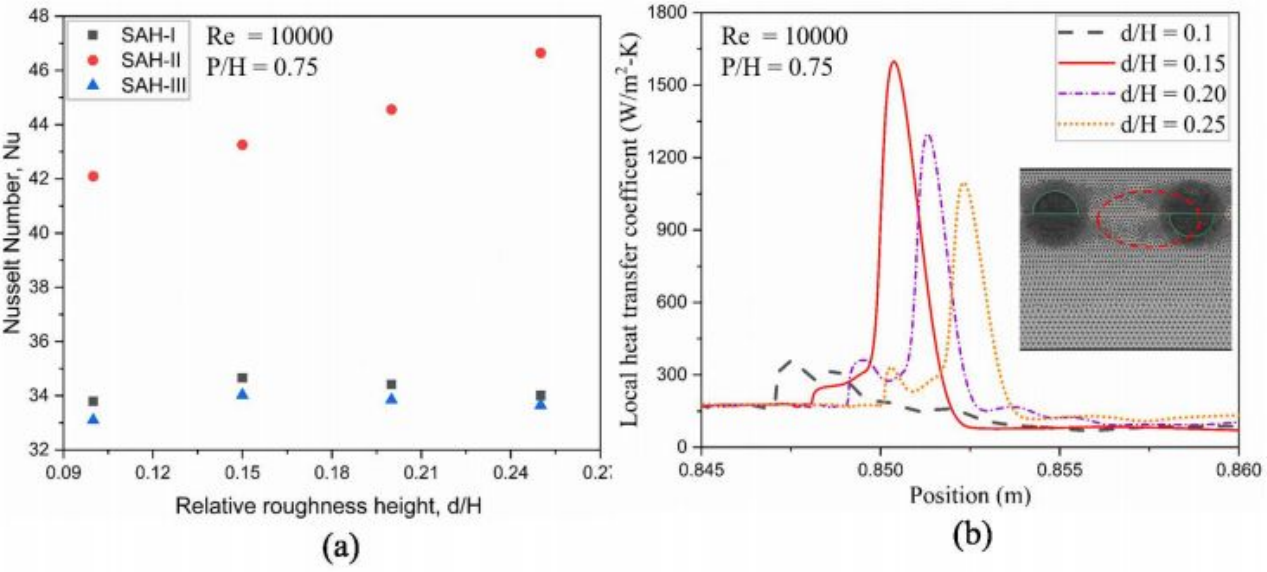

Figure 3.5: (a) Variation of Nusselt number with relative roughness height, (b) Variation of local heat transfer coefficient with position in SAH-I

3.3.2 *The effect of rib diameter*

In order to show the influence of ribs sizes on heat transfer with semicircular ribs, the variation of Nusselt number (Nu) with relative roughness height (d/H) of different types of SAH has been shown in Fig.3.5(a) for fixed value of Re= 10,000. The maximum value of Nusselt number in SAH-I and SAH-III is observed for $d/H = 0.15$. The values of Nusselt number for SAH-I and SAH-III with semicircular ribs for $d/H = 0.15$ are 8-12% and 4-7% higher than SAH-I and SAH-III with smooth absorber plate respectively. It can be seen that Nu increases to a maximum and

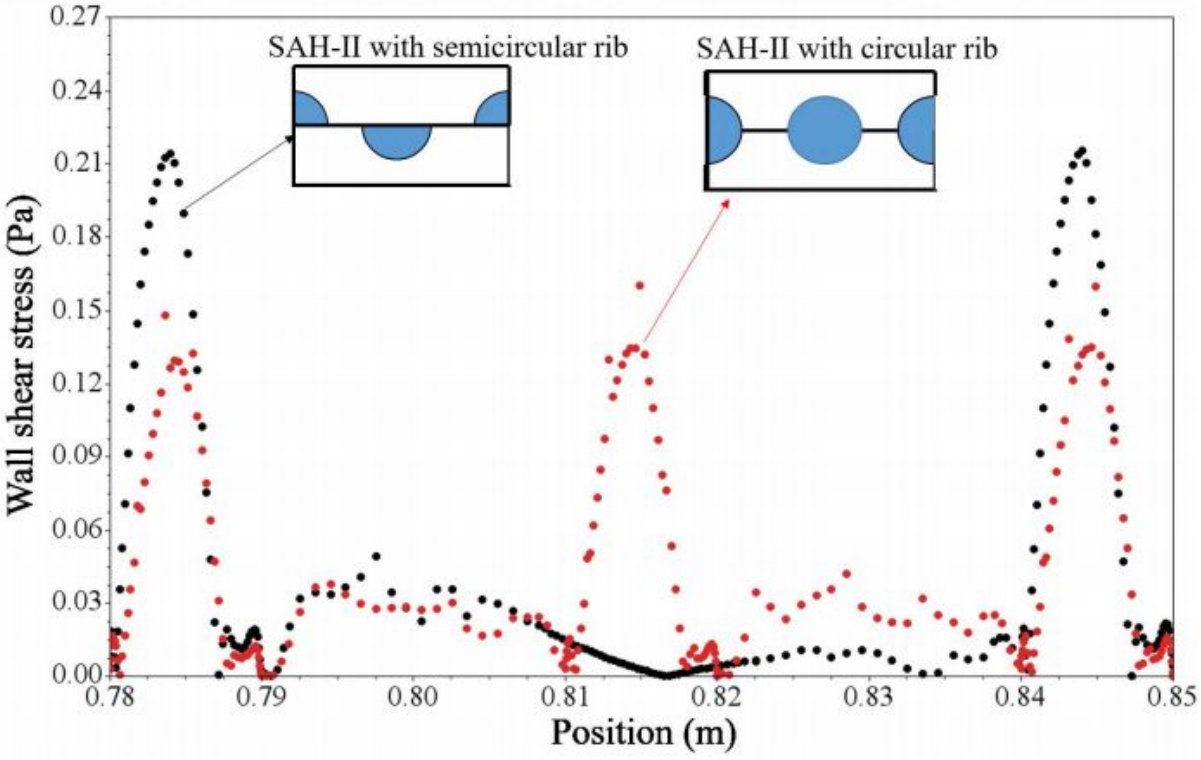

Figure 3.6: Variation of local wall shear stress in SAH-II with semicircular and circular ribs at high Re= 10,000 and $^{d}/_{H}$ =0.25.

then declines with increase in $^{d}/_{H}$. There is an optimum value of rib diameter at which thermal performance is higher. The highest and lowest value of Nu occurs at the $^{d}/_{H}$ value of 0.15 and 0.25, respectively. The value of Nusselt number increases with increase of $^{d}/_{H}$ in SAH-II and maximum value occurs for $^{d}/_{H}$ =0.25. This is due to equal mass flow rate split in upper and lower channel for SAH-II while unequal mass flow rates seen in upper and lower channels for SAH-I and SAH-III. Also, the variation of local heat transfer coefficient with position (along the absorber plate length) the upper channel in SAH-I for different values of $^{d}/_{H}$ is shown in Fig.3.5 (b). It is observed that the same trend of local heat transfer follows, as seen in Fig.3.5 (a). As the relative roughness height increases, the fluid impingement position also changes along the absorber length. Two peaks of the local heat transfer coefficient have been observed along the length of the absorber plate. The first peak appears due to the secondary recirculation zone just across the rib and the second peak due to the impingement of fluid along the length of the absorber plate. As a result, it effectively increases the overall heat transfer coefficient.

Fig. 3.8 shows the comparison of Nusselt number with respect to Reynolds number for SAH-II type designs with semicircular ribs for $^{d}/_{H}$ in the range 0.1-0.25 and SAH-II with smooth absorber plate. Significant enhancement in Nu has been observed. An increase in the $^{d}/_{H}$ ratio raises the Nu value due to generation of secondary vortices that mix the hot and cold fluid near the absorber plate. The maximum Nusselt number is obtained at $^{d}/_{H}$ =0.25, and minimum value

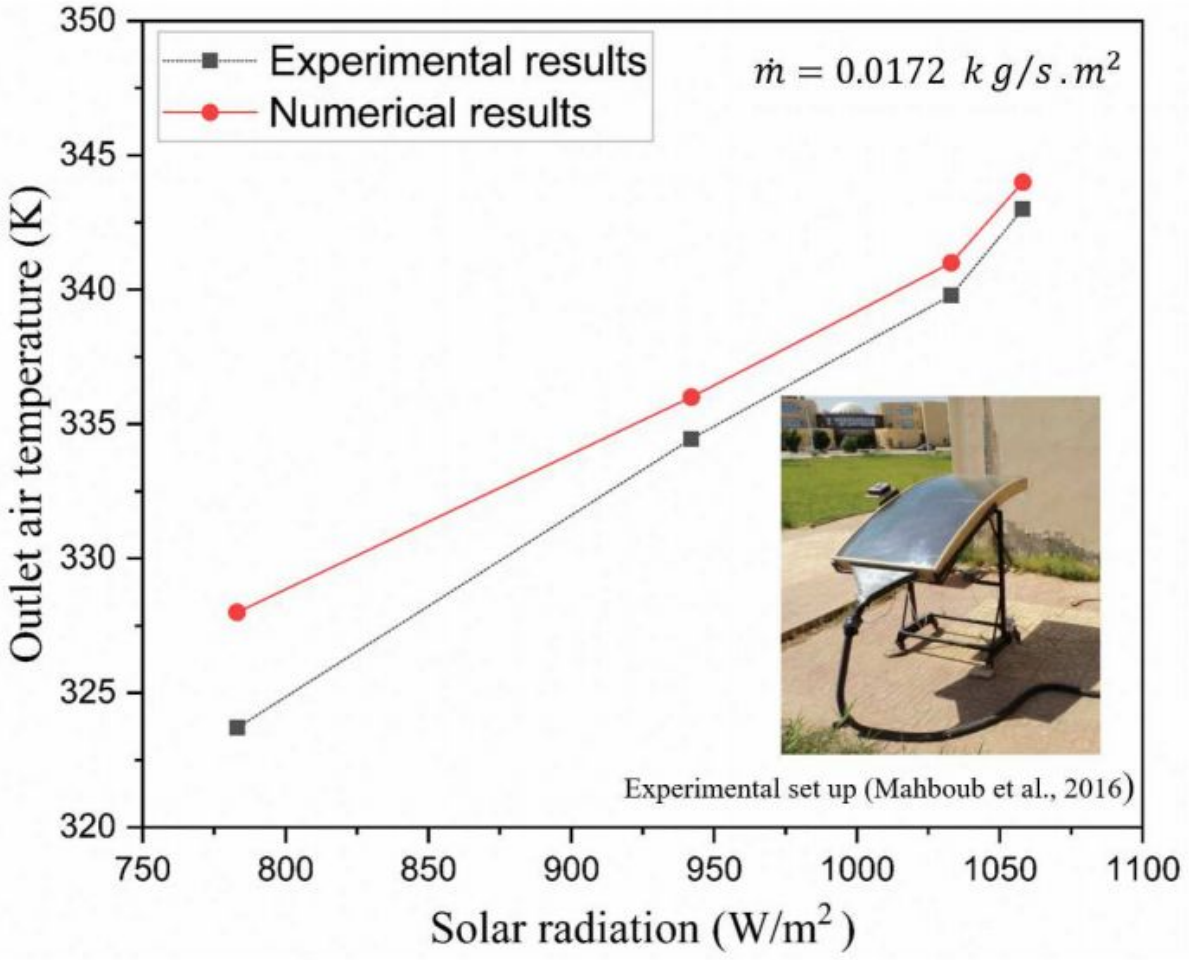

Figure 3.7: Comparison of experimental results with numerical values of outlet air temperature w. r.t solar radiation.

with the smooth absorber plate. The Nusselt number values for SAH-II with semicircular ribs for $^{d}/_{H}$ =0.25 are 41-44% higher than SAH-II with smooth absorber plate. Contours of turbulent kinetic energy and temperature provide further insight into the investigation of the heat transfer behavior as shown in Fig.3.9.The turbulent kinetic energy is high on the downstream side of the rib. It decreases as we move away from the absorber wall. With strong turbulence generated with the increase in the d/H ratio, an increase in average Nu values has also been observed (see Fig. 3.8).For example, when compared to smooth curved SAH, there is about 41-44% increase in Nu for $^{d}/_{H}$ =0.25. Similar observations for SAH-III type designs were also seen (figure not shown).

Thermal effectiveness (ε) is one of the most important thermal performance parameters of SAH, which is the fraction of actual heat received by fluid to maximum potential heat given to fluid by the absorber plate i.e.

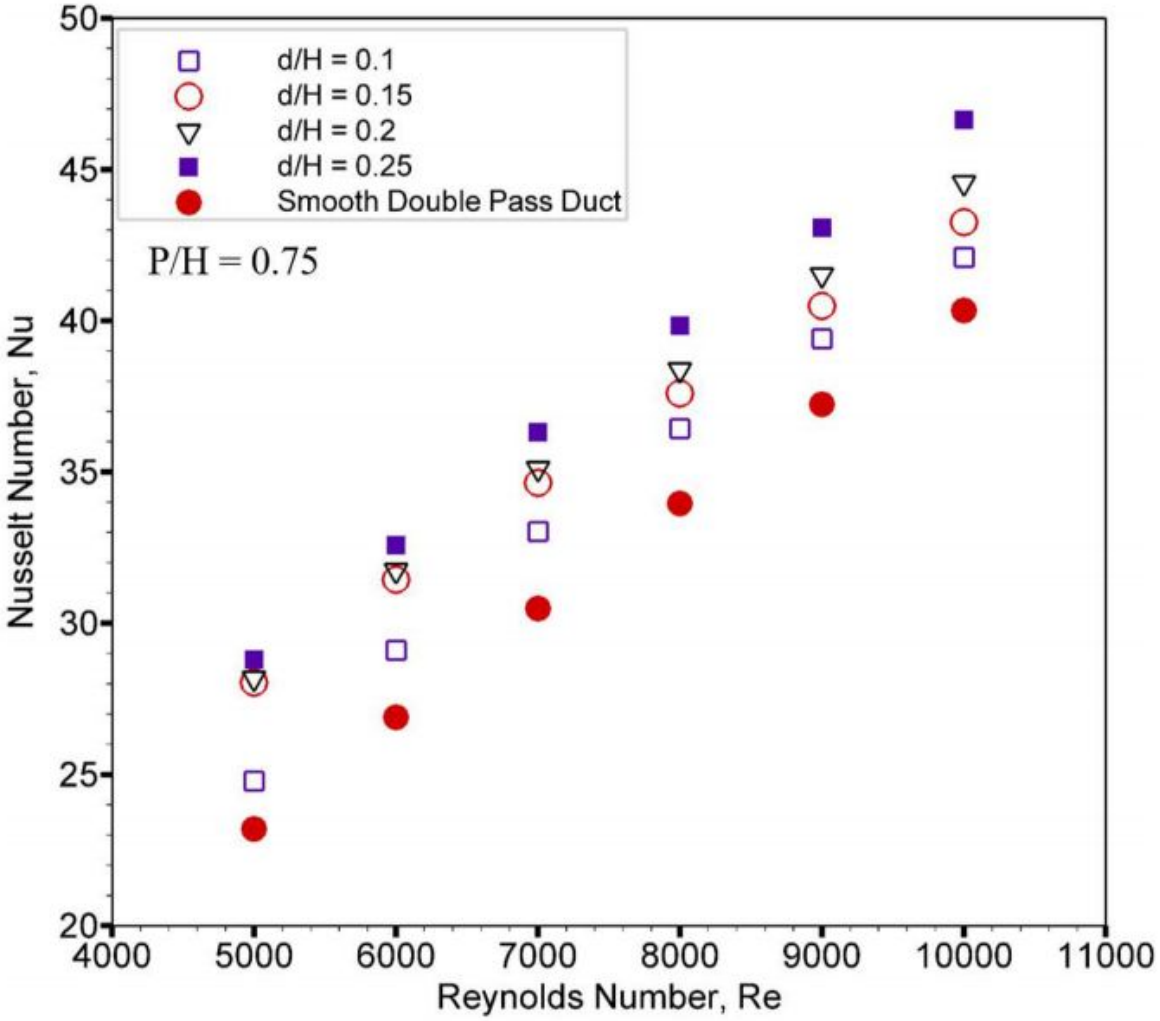

Figure 3.8: Variation of Nusselt number with Reynolds number for SAH-II.

$$\varepsilon = \frac{(T_0 - T_i)}{(T_p - T_i)} \tag{3.17}$$

Fig.3.10 (a) shows a plot of the ε versus Re for different SAH with semicircular ribs for different values of d/H in the range 0.1-0.25. It is found that the value of effectiveness declines with increasing values of the Re, in the range of parameters used. SAH-I with semicircular ribs shows the highest value of effectiveness at $d/H=0.15$ and the lowest value at $d/H=0.1$. The maximum enhancement of effectiveness is 1.20 times the flat duct for the same d/H ratio, Re = 5000. At higher Re, the interaction time of cold fluid with hot absorber plate decreases, and hence, the effectiveness of SAH also decreases. Fig.3.10 (b) shows the effect of thermal effectiveness as a function of Re for different values of d/H ratios for SAH-II type designs with semicircular and SAH-II with a smooth absorber design. A substantial enhancement in the thermal effectiveness of SAH-II equipped with semicircular ribs when compared to smooth flow passage is observed. The maximum percentage increase of 37.10% has been observed at the Reynolds number of 5000. This

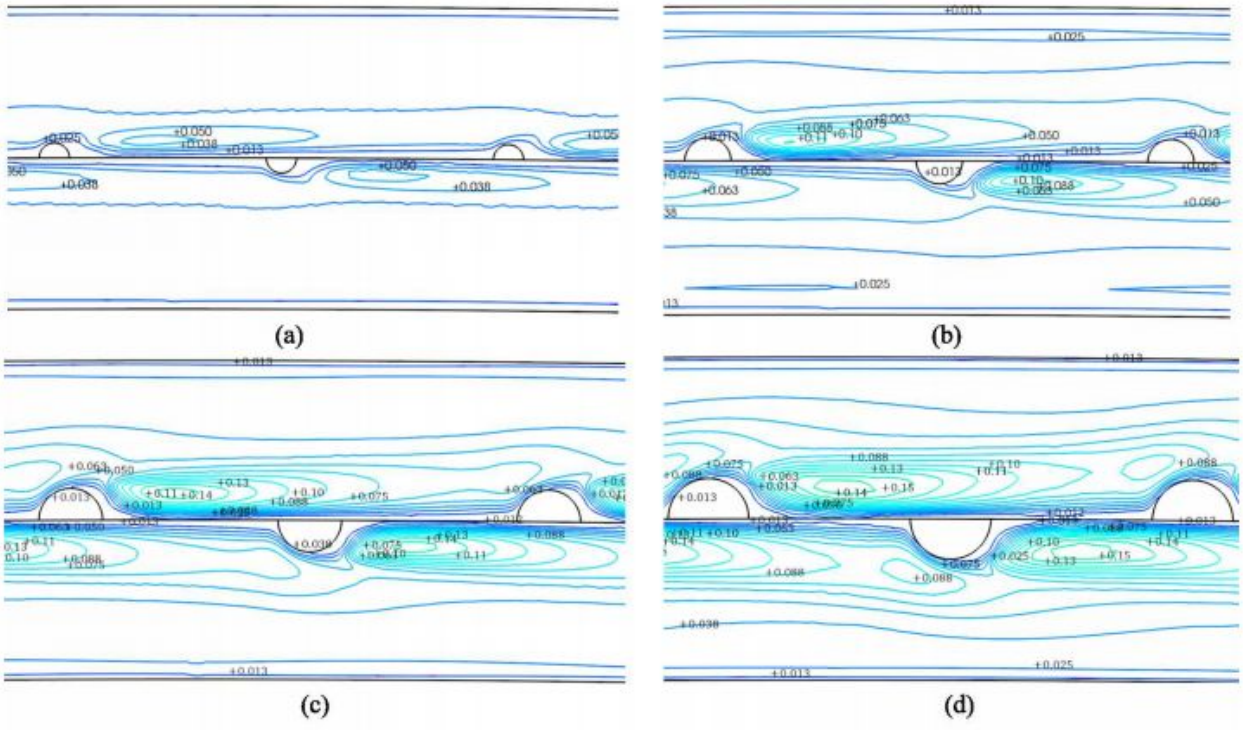

Figure 3.9: Contours of turbulent kinetic energy at $Re = 5000$ for fixed value of P/H and different value of relative roughness height (a) $d/H = 0.1$, (b) $d/H = 0.15$, (c) $d/H = 0.20$ and (d) $d/H = 0.25$.

substantial increase is due to secondary flow vortex formation, which gets further enhanced due to the curved nature of the SAH design. Fig.3.10 (c) shows the corresponding variation of effectiveness for SAH-III type designs. The maximum percentage increase in effectiveness with semicircular rib has been found 20.75% at d/H=0.2 and $Re = 5000$.

Thermal performance of SAH can also be explained in term of Stanton number (St); it is evaluated by the ratio of heat transferred into the fluid to the thermal capacity of fluid i.e.

$$St = \frac{Nu}{RePr} \tag{3.18}$$

To concise the manuscript, the variation of St in a different range of Re and d/H ratio for various designs of curved SAH has not been shown. It was observed that out of SAH-I, SAH-II and SAH-III designs, SAH-II (d/H =0.25, Re = 5000) showed maximum enhancement in St (by 24.13%) when compared to base design of smooth curved SAH, closely followed by SAH-III (12.96%) and SAH-I (12.46%).

The resistance offered to the fluid flow inside the SAH plays an essential factor in determining the pumping power requirement and overall operating cost [35, 44, 92, 125] Since SAH -II and SAH-III type designs show better thermal performance, results on friction factor variation is shown for SAH-II and SAH-III designs only (see Fig.3.11). It can be seen that friction factor

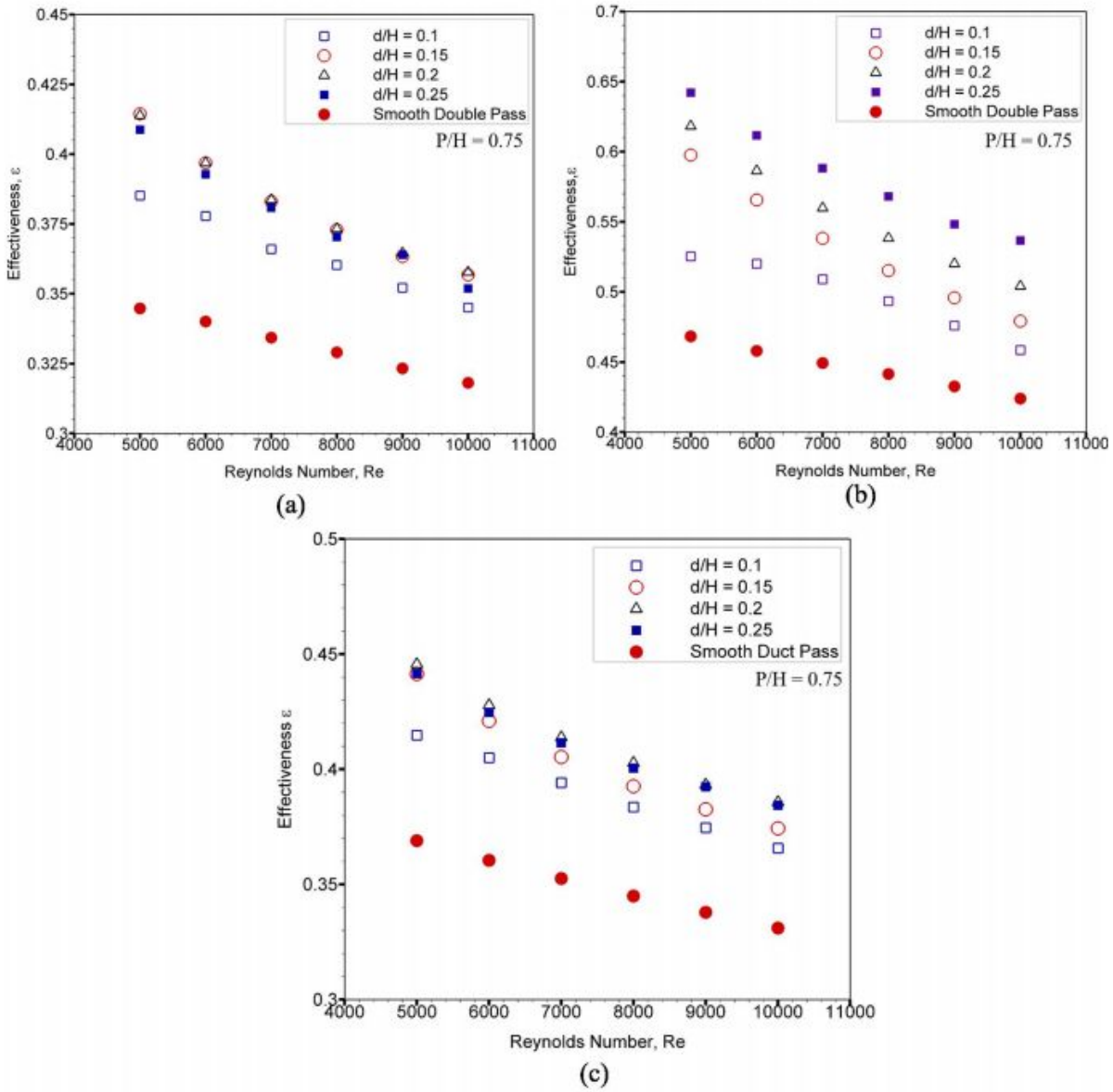

Figure 3.10: Variation of the effectiveness with Reynolds number (a) SAH-I, (b) SAH-II, and (c) SAH-III.

decrease with the increase of Reynolds number in all cases. As the value of $^{d}/_{H}$ increases, the strength of free shear layer to re-attach diminishes, thus producing a relatively poor improvement in the heat transfer coefficient. At the same time, a significant gain in the friction factor was observed. The maximum value of the friction factor is seen at $^{d}/_{H}$ =0.25 and Re = 5000, and it is 2.73 times that of the flat duct SAH. Fig.3.11 (b) shows that the average friction factor for SAH-III with semicircular ribs. In this case, the friction factor is 2.29 times that of the smooth SAH-III for $^{d}/_{H}$ of 0.25 and Re of 5000.

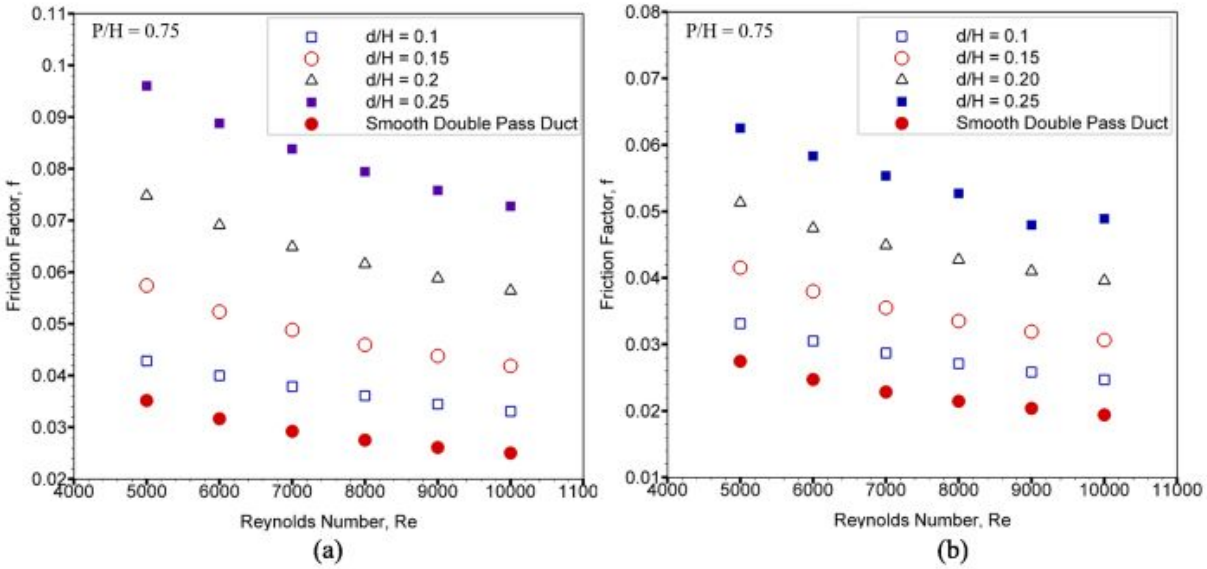

Figure 3.11: The effect of Reynold number on friction factor for different SAH (a) SAH-II, and (b) SAH-III.

3.3.3 *Effect of absorber plate location*

The location of the absorber plate in a DPSAH plays a significant role in enhancing the overall thermal performance [31, 147]. In order to show the influence of location, the temperature contour of SAH-I with semicircular rib (y/H =0.25, absorber plate near top glass), SAH-II with semicircular rib (y/H =0.50, absorber plate in middle) and SAH-III with semicircular rib (y/H =0.75, absorber plate near bottom insulated plate) at fixed value of operating parameter are shown in Fig.3.12. The lower scale of temperature is kept the same in all the figures for insightful visual comparison. The enlarged section at both inlet and outlet has been shown as an inset in the figures. It can be seen that when a plate is near the top glass (Fig.3.12(a)), heat transfer is mainly dominated by thermal diffusion as most of the fluid in the upper duct is at a significantly higher temperature compared to the bottom passage. The significant effect of diffusion in the bottom passage is seen only near the end of the duct. The majority of the fluid flowing underneath passage without interaction with the hot absorber plate. In case when absorber plate is placed at the center (Fig.3.12(b), SAH-II), heat transfer seems to be more uniform on both the sides of the heated plate, and hence, the uniform temperature distribution is observed. When the heated absorber plate is moved down towards the bottom insulated plate (Fig.3.12(c), SAH-III), similar observations on thermal diffusion effect are seen as in the case when the plate was near the top glass. However, the thermal diffusion effect is confined below the absorber plate, just opposite the case of SAH- I case. Even though similar thermal effects are seen in SAH-I and SAH-III, heat transfer from SAH-II was observed to be higher than the SAH-I case. One reason is that the heated fluid from the absorber plate rises due to buoyancy effect and thus, allows heated air to

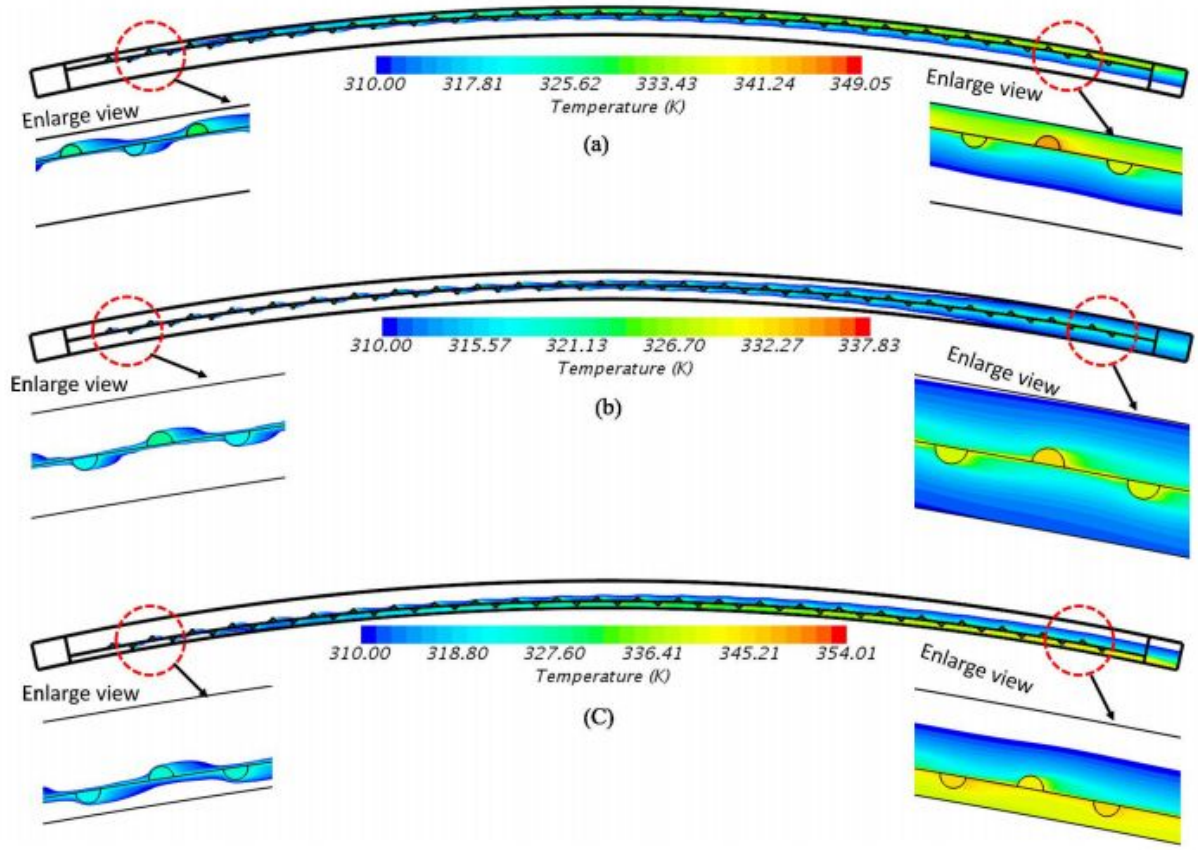

Figure 3.12: Temperature contour at Re = 10,000 at fixed value of d/H =0.25, P/H = 0.75 and different relative location of absorber plate (a) SAH-I (i.e., y/H =0.25) (b) SAH-II (i.e., y/H =0.50), and (c) SAH - III (i.e., y/H =0.75).

mix with the cold fluid. In the SAH-I case, heated fluid shows a tendency to lose more heat to the environment due to the proximity of the glass. SAH-II provides the highest outlet air temperature, followed by SAH-III and SAH-I. In quantitative term, SAH-II type designs with semicircular ribs (y/H =0.50) shows by about 5°C higher outlet temperature than SAH-I designs (y/H =0.25) at Re = 5000.

The effect of the vertical location of the absorber plate can be studied from the local variation of temperature across the depth. The temperature variation with position (along with duct height) has been shown in Fig.3.14 for different types of SAH with semicircular ribs at the central location of the duct. It is seen that temperature of fluid increases initially and then decreases in all types of SAH. The peak temperature is at the absorber location. It is also clear that heat transfer rate equally occurs on both sides of the absorber in SAH-II while larger heat removal occurs in the lower and upper channel of SAH-III and SAH-I, respectively. As a result, SAH-I dissipate more heat to the environment as compare to SAH-II and SAH-III.

As seen earlier, air is split unevenly between the upper and lower channel. How does this split effect the outlet temperature? Outlet air temperature is the manifestation of dynamics in-

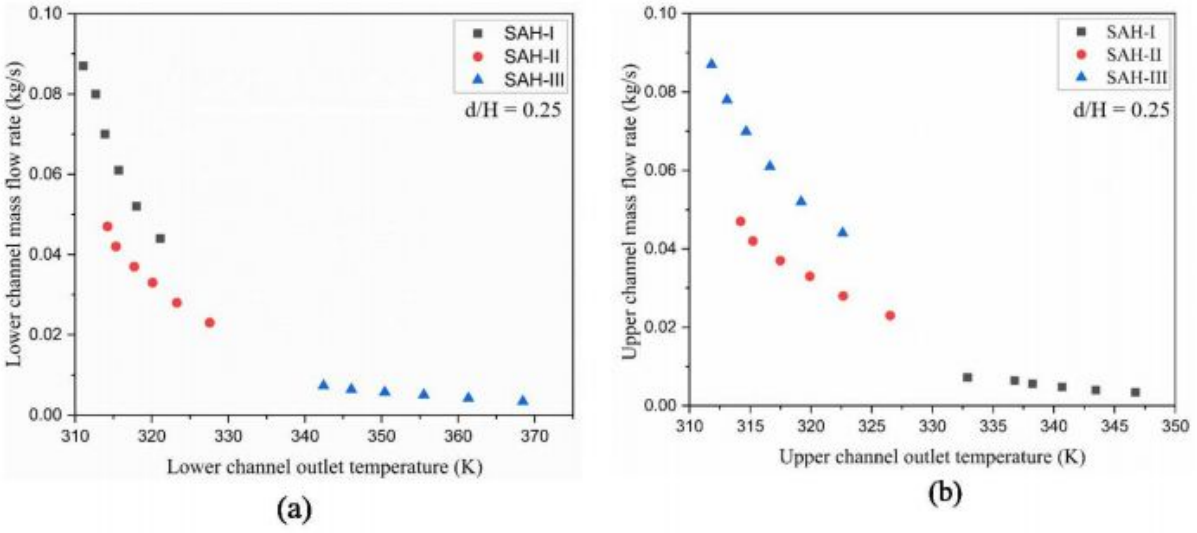

Figure 3.13: The variation of mass flow rate with outlet temperature (a) Lower channel (b) Upper channel.

side the channel. Fig.3.13 shows the outlet air temperature variations as a fraction of mass flow rate in the corresponding channels with semicircular ribs. Mass flow rates corresponds to the six values of Reynolds numbers used (5000-10000). Following points to be noted: (1) In SAH-II (collector placed at the center), there is equal split in air mass flow rates and hence the temperature variations in both upper and lower channel are equal, (2) In case of SAH-I, lower channel allows more ass flows and consequently show lower outlet temperature. Upper channel shows just opposite behavior, and (3) Variations in mass flow rate and temperature in SAH-III design is just opposite of SAH-I design. For example, higher mass flow rate (and lower temperature) was absorbed in the upper channel of SAH-III while lower mass flow rate (higher temperature) was observed in SAH-I the upper channel. From the above discussion it is clear that system resistances, location of collector and curvature of SAH plays an important role in the overall system performance.

3.4 Correlation development

From the results discussed above, it is clear that SAH-II type designs exhibit better thermal and hydraulic performance when compared to the other designs. It was also observed that thermo-hydraulic performance, i.e., $Nu-f$ for any designs of SAH, is a strong function of flow parameter Dean number or the Reynolds numbers and geometrical parameter roughness ratio ($^{d}/_{H}$). Thus, Nusselt number and friction factor in term of D_n and $^{d}/_{H}$ can be written as,

$$Nu = f_n\,(D_n, {}^{d}/_{H}) \tag{3.19}$$

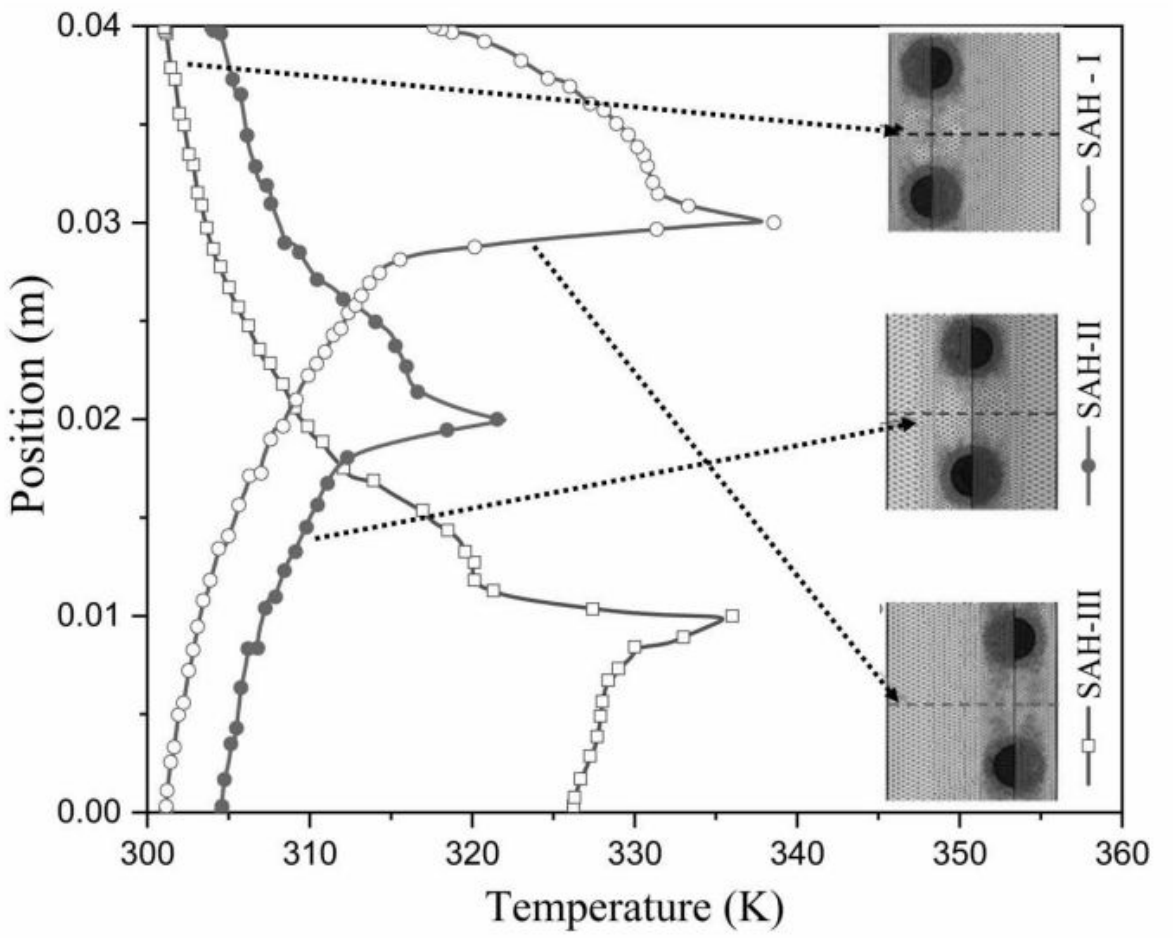

Figure 3.14: Variation of temperature with position (along with the duct height) at the central location of different SAH with semicircular rib at a fixed value of Re = 10,000 and $d/H = 0.25$. The location along the duct height is shown in the inset

$$f = f_n\,(D_n, d/H) \tag{3.20}$$

The functional form of Nu and f variation will be derived from the data generated for various designs of SAH -II discussed above.

3.4.1 *Correlation for* Nu

Variations in Nu with D_n is shown in Fig.3.15. A straight-line fit show that the nature of variation is exponential.

The regression analysis of these data points is fitted by a straight line, which has the form:

$$Nu = A_0 D_n^{0.69} \tag{3.21}$$

The coefficient A_0 depends on another operating parameter $^{d}/_{H}$ ratio. Taking $^{d}/_{H}$ into consideration and plotting all the data of A_0against $^{d}/_{H}$, a new relationship was derived. The regression analysis has the following expression

$$ln\left(\frac{Nu}{D_n^{0.69}}\right) = ln\,(B_0) + B_1\,ln\,(^{d}/_{H}) + B_2\left[\{ln\,(^{d}/_{H})\}^2\right] \tag{3.22}$$

equation (22) can be rearranged as

$$Nu = B_0 D_n^{0.69}\,(^{d}/_{H})^{0.05}\,exp\left[-0.0165\,\{ln\,(^{d}/_{H})\}^2\right] \tag{3.23}$$

The value of the coefficients is obtained as given below

$A_0 = 0.39$and $B_0 = 0.44$

The final expression for N has the form:

$$Nu = 0.44 D_n^{0.69}\,(^{d}/_{H})^{0.05}\,exp\left[-0.0165\,\{ln\,(^{d}/_{H})\}^2\right] \tag{3.24}$$

Note that only the coefficient 0.44 will change to 0.0923 if D_n is replaced by Re in above correlation.

3.4.2 *Correlation for* f

The friction factor relation with D_n and geometrical parameter $^{d}/_{H}$ratio has been obtained by the same procedure as discussed above. And the variation is shown in Fig.3.16.

The final expression for the friction factor is written as

$$f = 16.4 D_n^{-0.406}\,(^{d}/_{H})^{2.5}\,exp\left[0.44\,\{ln\,(^{d}/_{H})\}^2\right] \tag{3.25}$$

Only the coefficient value 16.4 will change to 41.67 in above correlation if D_n is replaced by Re.

Fig.3.17 and Fig.3.18 illustrates the comparison of numerical data of Nu and f with the predicted value from the developed correlations. The absolute percentage deviation in the predicted data from the numerical data of Nu and friction factor is 3.42% and 0.87%, respectively. Low deviation in the predicted data suggests that the developed correlations can be used with reasonable accuracy to forecast Nu and f variation in curved DPSAHs.

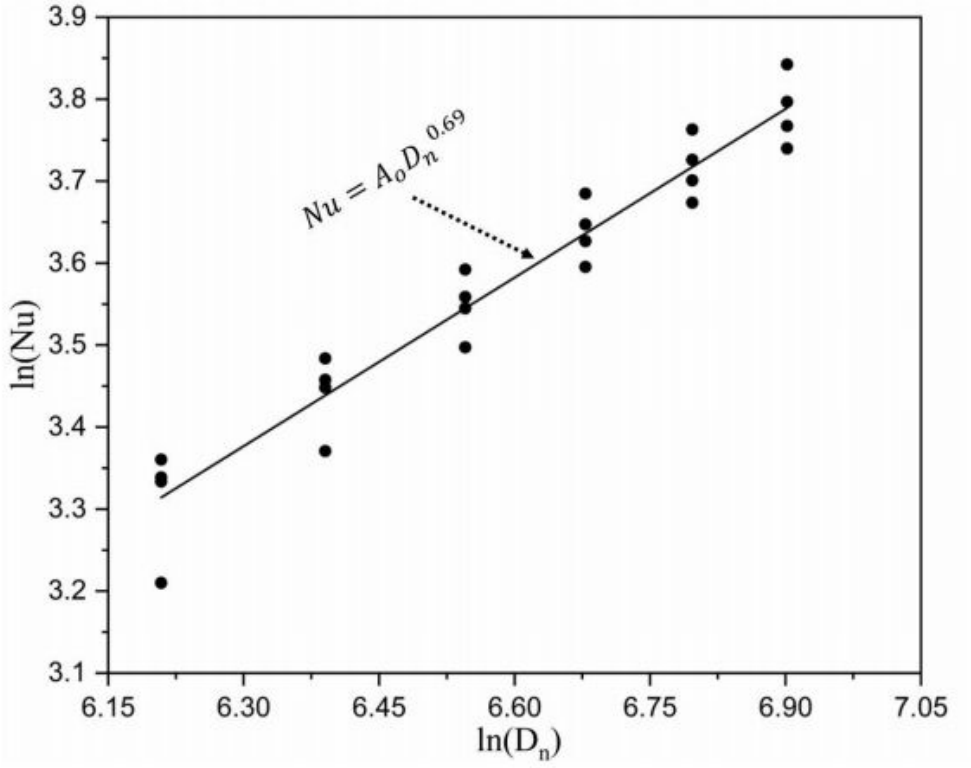

Figure 3.15: Variation of ln (Nu) as a function of ln (Dn).

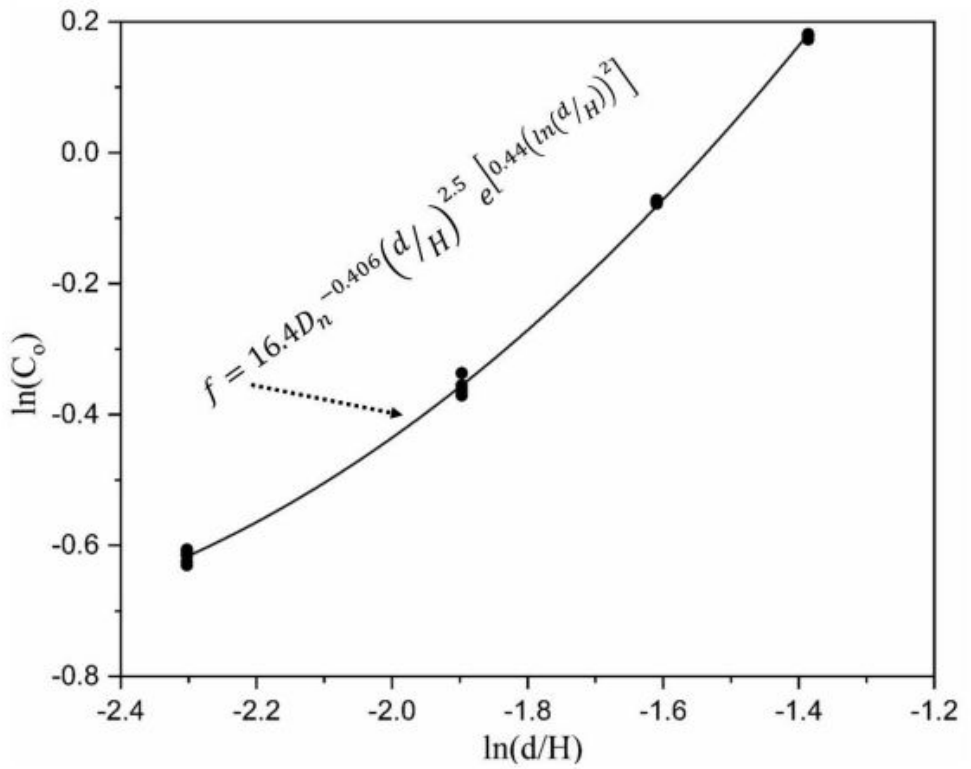

Figure 3.16: Variation of ln (C_0) with $ln\,(D_n)$.

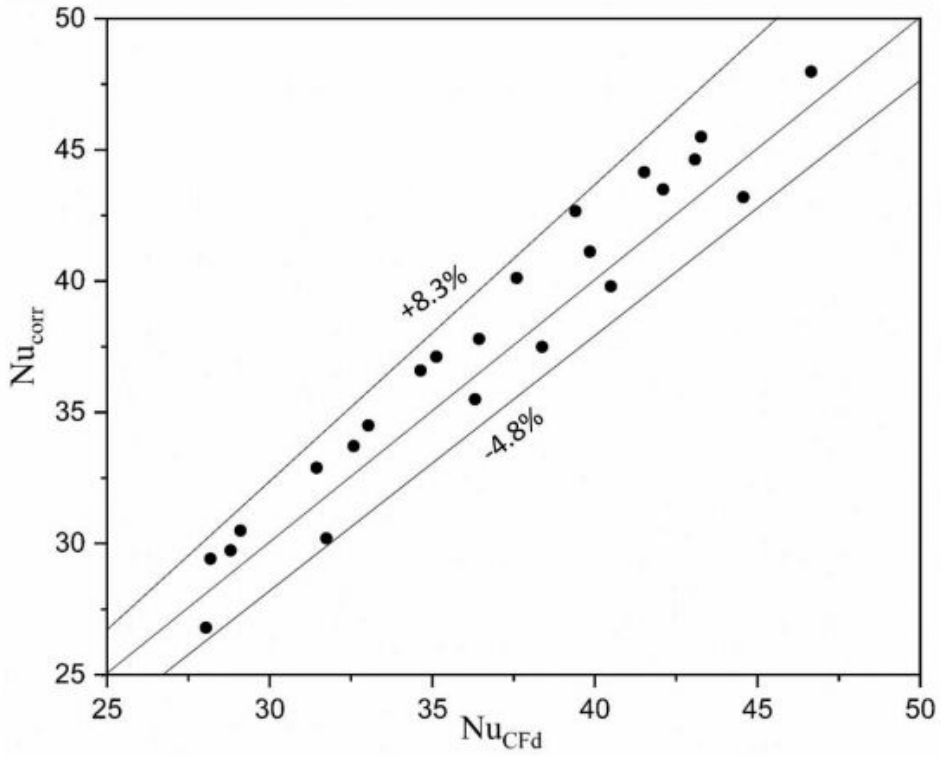

Figure 3.17: Comparison of numerical and predicted values of Nusselt number.

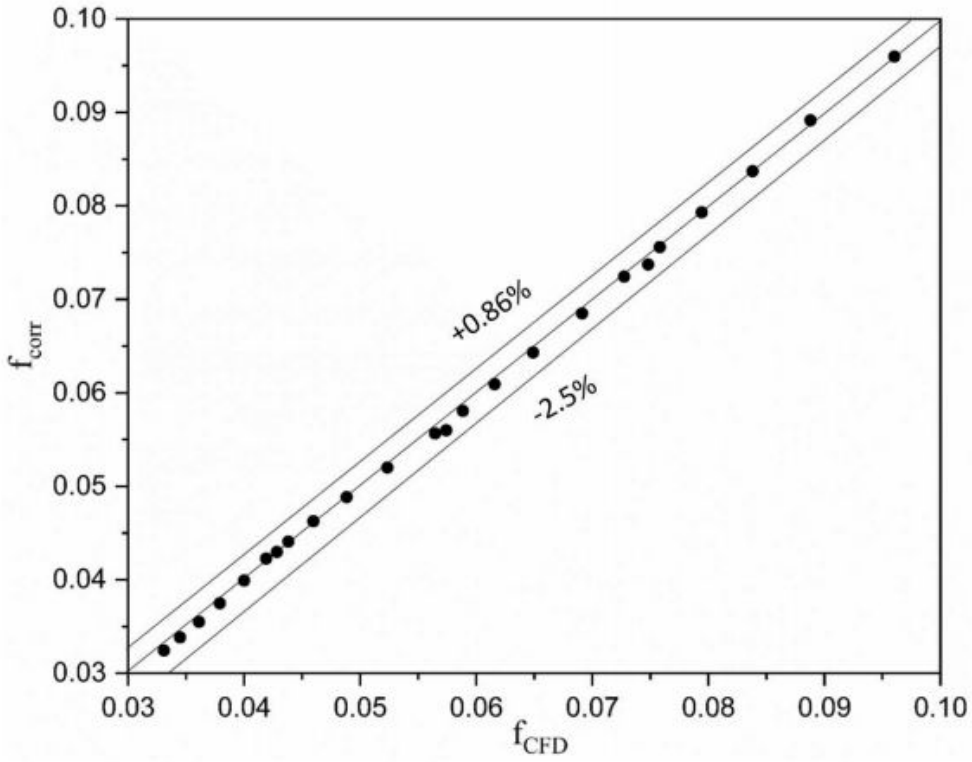

Figure 3.18: Comparison of numerical and predicted values of the friction factor.

3.5 Conclusions

Thermo-hydraulic performance characteristics of a curved design double pass solar air heater (DPSAH) has been investigated numerically under various ranges of Reynolds number, relative roughness ratio (d/H), and position of absorber plate (y/H). Following are the critical observations from the study:

- Asymmetric semi-circular extended surfaces or ribs show better thermal and hydraulic performance than symmetric circular ribs. High energetic vortices reattach with the heated absorber plate frequently and thus show higher thermal performance with semi-circular ribs.

- Thermal effectiveness of curved DPSAH equipped with semicircular ribs shows by about 37% enhancement when compared to smooth flow passage at $Re = 5000$. This substantial increase is due to secondary flow vortex formation, which gets further enhanced due to the curved nature of the SAH design.

- For best thermal performance, the maximum roughness height of the extended surfaces can be 25% of the duct height, i.e., for $^{d}/_{H}$ =0.25, enhanced heat transfer was observed with lower hydraulic losses.

- Placing the observer plate at mid of the insulating wall and transparent glass cover shows higher thermal performance, i.e., about 5°C higher outlet temperature was observed compared to other positions.

- Two independent correlations were developed for Nusselt number and friction factor variations with Dean numbers and relative roughness height. The nature of variation is exponential, and it has the form: $Nu = k_1 D_n^{k_2} \left(^{d}/_{H}\right)^{k_3} exp\left[k_4 \{ln\left(^{d}/_{H}\right)\}^2\right]$.

- The predicted Nusselt number and friction factor from the developed correlations agrees reasonably well with the data with a maximum deviation of 3.42% and 0.87%, respectively.